



## Original Research

## Single-cell RNA sequencing analysis revealed cellular and molecular immune profiles in lung squamous cell carcinoma

Bo Hao<sup>a,1</sup>, Ziyao Zhang<sup>a,1</sup>, Zilong Lu<sup>a,1</sup>, Juan Xiong<sup>a,1</sup>, Tao Fan<sup>a</sup>, Congkuan Song<sup>a</sup>, Ruyuan He<sup>a</sup>, Lin Zhang<sup>a</sup>, Shize Pan<sup>a</sup>, Donghang Li<sup>a</sup>, Heng Meng<sup>a</sup>, Weichen Lin<sup>a</sup>, Bin Luo<sup>b</sup>, Jinfeng Yang<sup>c</sup>, Ning Li<sup>a</sup>, Qing Geng<sup>a,\*</sup>

<sup>a</sup> Department of Thoracic Surgery, Renmin Hospital of Wuhan University, Wuhan 430060, China

<sup>b</sup> Department of Pathology, Renmin Hospital of Wuhan University, Wuhan, China

<sup>c</sup> Department of Pathology, Xiangyang Central Hospital, Affiliated Hospital of Hubei University of Arts and Science, Xiangyang, China

## ARTICLE INFO

## Keywords:

Lung squamous cell carcinoma  
Single-cell sequencing  
Tumor microenvironment  
Immune landscape

## ABSTRACT

Although breakthroughs have been made in the treatment of non-small cell lung cancer, there are only a few choices for advanced-stage or recurrent lung squamous cell carcinoma (LUSC) patients. In our study, we identified 7 major cell types in the depicted immunolandscape of LUSC microenvironment using single-cell RNA sequencing. We found that an immunosuppressive receptor, T cell immunoglobulin and immunoreceptor tyrosine-based inhibitory motif domain (TIGIT), was highly expressed by regulatory T cells (Tregs) and exhausted CD8<sup>+</sup>T cells, suggesting that upregulation of TIGIT might promote an immunosuppressive microenvironment and inhibit the cytotoxic ability of CD8<sup>+</sup>T cells. We also identified tumor-associated neutrophil (TAN), characterized by CXCR2, CSF3R and CXCL8, in the tumor region, and TANs upregulated the expression of interleukin 1 receptor antagonist (IL1RN) which suggested that TAN might exert an immunosuppressive role via expressing IL1RN. Furthermore, the number of SPP1<sup>+</sup> macrophages (SPP1<sup>+</sup>M) significantly increased in tumor microenvironment, which was correlated with the poor survival of patients. Additionally, regulatory networks based on SPP1<sup>+</sup>M revealed that the disparities of several ligand-receptor pairs existed between tumor and normal tissues. Among these pairs, SPP1-CD44 showed the most interactions between SPP1<sup>+</sup>M and other cell types. Our results provided deep insight into the immune landscape of LUSC and an essential resource for drug discovery in the future.

## Introduction

Lung cancer is one of the most common cancers worldwide and has been the leading cause of cancer-related mortality [1]. Non-small cell lung cancer (NSCLC) is mainly categorized as lung adenocarcinoma (LUAD) and lung squamous cell carcinoma (LUSC), and LUSC accounts for approximately 30% of new NSCLC cases [2]. However, unlike LUAD, patients with inoperable LUSC only have a few choices to prolong their lifetime.

The tumor microenvironment (TME) is an interactive and co-evolving dynamic environment composed of tumor cells, immune cells, stromal cells, and extracellular matrix, and takes an essential part in oncogenesis and tumor progression [3]. Lung cancer is characterized by its high variations of the TME, which determines the responsiveness

and tolerance of immunotherapy [4]. The emergence of single-cell RNA sequencing (scRNA-seq) provided an unprecedented view of how various cells consist of heterogeneous and phenotypically diverse populations within tumors. Compared with conventional 'bulk' RNA-sequencing, scRNA-seq profiles the gene expression pattern at the single-cell level, and provides deep insights into the TME as well as cell-cell interactions, which may facilitate discovering the potential targets of novel cancer therapies [5]. Several studies deeply investigated the TME and depicted cell atlases of lung adenocarcinoma [6–9]. However, few studies tried to reveal the TME of LUSC and draw a blueprint of TME [9].

In our study, we extracted single-cell RNA sequencing data from LUSC patients deposited in GEO datasets to characterize the TME and drew a comprehensive blueprint of the immuno-landscape. We aimed to

\* Corresponding author.

E-mail address: [gengqingwhu@whu.edu.cn](mailto:gengqingwhu@whu.edu.cn) (Q. Geng).

<sup>1</sup> These authors contributed equally to this work.

investigate molecular features, signaling pathways, and cell-cell interactions that contribute to tumor progression in primary LUSC.

## Materials and methods

### Human tumor specimens for immunohistochemical staining and immunofluorescence

Human tissue specimens were obtained from the Renmin Hospital of Wuhan University under an approved Institutional Review Board protocol, and all participants provided written informed consent. A total of 65 samples of primary I-IIIa LUSC patients (without radiotherapy, chemotherapy, or immunotherapy before surgery) were included in our study from 2013-2015 at the Renmin Hospital of Wuhan University (Supplementary Table 1). Follow-up was performed through telephone interviews. Recurrent free survival (RFS) was the primary endpoint, which was defined as the interval between the date of the resection and the date of recurrence.

### Single-cell sequencing data

RNA-sequencing data of LUSC patients were extracted from the GSE127465 [10] and GSE117570 [11] in the GEO database and E-MTAB-6149 and E-MTAB-6653 in ArrayExpress database [8]. This included 6 LUSC tissue samples (1 from GSE117570, 2 from GSE127465, 3 from E-MTAB-6149 and E-MTAB-6653) and 9 normal tissue samples (3 from GSE127465 and 6 from E-MTAB-6149 and E-MTAB-6653).

The raw data was obtained, and processed by the Seurat (v 4.0.4) [12] R package for downstream analysis. Quality control was performed to remove the low-quality cells according to the criteria (unique molecular identifiers (UMIs) and gene count) reported in the original paper. Additionally, cells that have over 15% UMIs derived from the mitochondrial genome and 40% derived from the ribosomal genome were discarded.

### Dataset integration and joint analysis

After filtering, all datasets were combined for further analyses. The “IntegrateData” function was performed potential batch effect, and then, batch-corrected integrated data was obtained [12]. Then, the “ScaleData” function was performed to ensure that the expression of all genes was given equal weight in the downstream analyses and that highly expressed genes were not dominant. Next, principal component analysis (PCA) was performed for 50 principal components.

### Pathway analysis

High variable genes of cell subgroups were calculated by the “FindAllMarkers” function in the Seurat package. Gene set variation analysis (GSVA) and gene set enrichment analysis (GSEA) analysis was performed with the GSVA and GSEA package, respectively, on a matrix of functional genes downloaded from the MSigdb database (<http://software.broadinstitute.org/gsea/index.jsp>). Differences in pathways between different cell groups were calculated with a linear model offered by the Limma package.

### Cell-cell interaction network

CellPhoneDB 2 [13,14] was used to establish the receptor-ligand pairs onto our cell subsets within tissues of each origin to identify cell-cell interactions. CellPhoneDB 2 is a Python-based computational analysis tool, which enables the analysis of cell-cell communication at the molecular level.

### Correlation to TCGA data

Bulk RNA sequencing data, as well as corresponding clinical information in TCGA LUSC databases, were also obtained from UCSC XENA (<https://xena.ucsc.edu/>). Survival endpoint inTCGA: overall survival (OS), which is defined as the period from the date of diagnosis until the date of death from any cause, and disease-specific survival (DSS), which is defined as the period from the date of diagnosis until the date of death due to LUSC.

To estimate the relative abundance of the cell subclusters identified in single-cell profiles for LUSC, CIBERSORTx [15] was performed according to the tutorials on the website (<https://cibersortx.stanford.edu/>).

### Immunofluorescence and immunohistochemistry staining

Patient tissue samples were collected after the tumor resection. And it was fixed in 10% formalin, and then embedded in paraffin. Thereafter, 4- $\mu$ m-thick sections were prepared.

The following antibodies were used to detect specific proteins: anti-CD4 (rabbit, 1:200, Abcam, ab183685, Cambridge, UK), anti-TIGIT (rabbit, 1:200, Abcam, ab243903, Cambridge, UK), anti-FoxP3 (rabbit, 1:200, Servicebio, GB11093, Wuhan, China), anti-LAG3 (rabbit, 1:100, Abcam, ab254578, Cambridge, UK), and anti-CD8 (rabbit, 1:100, Abcam, ab217344, Cambridge, UK), anti-S100A8 (rabbit, 1:300, Proteintech, 66853-1-Ig, Wuhan, China), anti-CD68(mouse, 1:50, Santa, SC-20060, Texas, USA), anti-CD206(rabbit, 1:100, Proteintech, 18704-1-AP, Wuhan, China), anti-CXCR2(rabbit, 1:100, Abcam, ab225732, Cambridge, UK), and anti-CSF3R(rabbit, 1:100, Cusabio, PA860321, Wuhan, China), anti-IL1RN(rabbit, 1:100, GeneTex, GTX106490, California, USA), anti-PDGFRB (rabbit, 1:100, Invitrogen, PA1-30317, California, USA), anti-RGS5 (rabbit, 1:50, Proteintech, Cat. No.11590-1-AP, Wuhan, China), anti-osteopontin(rabbit, 1:50, Proteintech, Cat. No. 22952-1-AP, Wuhan, China) and anti-SMA(rabbit, 1:50, Proteintech, Cat. No. 14395-1-AP, Wuhan, China). And the corresponding secondary antibodies used in our study, including Alexa Fluor  $\text{\textcircled{R}}$  488 goat anti-Mouse IgG (H&L, 1:1000), Alexa Fluor  $\text{\textcircled{R}}$  488 goat anti-Rabbit IgG (H&L, 1:1000), Alexa Fluor  $\text{\textcircled{R}}$  555 goat anti-Mouse IgG (H&L, 1:1000), Alexa Fluor  $\text{\textcircled{R}}$  555 goat anti-Rabbit IgG (H&L, 1:1000), Alexa Fluor  $\text{\textcircled{R}}$  680 goat anti-Mouse IgG (H&L, 1:1000), Alexa Fluor  $\text{\textcircled{R}}$  680 goat anti-Rabbit IgG (H&L, 1:1000).

Immunohistochemical staining analysis was performed by two experienced pathologists. They independently analyzed the expression of markers, and scored the intensity of expression(color of staining) [0 (no expression), 1 (weak expression (faint yellow)), 2 (moderate expression(claybank)) or 3 (strong expression(tan))] as well as the distribution of expression [0-5% (cells stained), 1 (5-25% of cells stained), 2 (26-50% of tumor cells stained), 3 (51-75% of tumor cells stained) or 4 (>75% of tumor cells stained)]. According to the total score (multiplying the intensity score by the distribution score), each patient was classified into one of four groups: negative (0), weak-positive (1-4), positive (5-8) group, or strongly positive group (9-12).

Parts of immunohistochemistry images in the study were obtained from the human protein atlas (HPA) (<https://www.proteinatlas.org/>), which provided large amounts of transcriptomics and proteomics data in specific human tissues [16].

## Results

### Analysis of single-cell transcriptomic profiling from LUSC and normal tissues

A total of 15 samples which originated from 13 individuals, including 9 normal and 6 tumor tissue samples, were obtained for analyses, and other detailed clinical characteristics were also presented in Supplementary Table 2. After being batch-corrected, we integrated the

single-cell transcriptomic data for a t-SNE-based cell clustering analysis. Overall, we obtained 39,574 single-cell transcriptomic profiles which were cataloged into 28 distinct cell clusters (Fig. 1a). Of these, 10,810 were derived from primary tumor tissue and the rest from normal lung tissues (Fig. 1b). Subsequently, according to established canonical marker gene expression (Supplementary Fig. 1 and Supplementary Table 3), we annotated these clusters as epithelial(EPCAM, SFTPA1, AGER, and KRT18), endothelial(PECAM1 and VWF), fibroblast (COL1A2), B/plasm (CD79A and IGHG1), mast(MS4A2), myeloid (CD68 and LYZ) and lymphocyte (T)/natural killer (NK) (CD3D, TRBC1, FCGR3A and KLRD1) cells (Fig. 1c). The frequency and proportion of each group from tumor and normal tissues were presented in Fig. 1d-f. Importantly, when comparing between patients, the proportion of each cell sub-cluster was of high variation (Fig. 1d, e). We also found that myeloid and T/NK cells were the most prevalent cell types in LUSC and normal lung tissues.

*T-cell transcriptome profiles suggested promising immunotherapy targets for LUSC*

T cell was the executors of the immune response, which was crucial important for immunotherapy. To delineate a detailed landscape of T/NK subclusters, 13,877 identified T/NK cells (accounting for .35.1% of all cells) were re-clustered, and 9 distinct cell clusters were obtained (Fig. 2a). According to established markers (Supplementary Table 3 and Supplementary Fig. 2A and B), C0 cluster was identified as CD4<sup>+</sup>/CD8<sup>+</sup>T, C1 as naïve CD4<sup>+</sup>T, C2 and C7 as CD8<sup>+</sup>effector T, C3 as exhausted CD8<sup>+</sup>T, C4 as HAVCR2<sup>+</sup>NK, C5 as regulatory CD4<sup>+</sup>T(Treg), C6 as proliferating T and C8 as XCL1<sup>+</sup>NK (Fig. 2c). Fig. 2b and 2d

presented the frequency and proportion of each cell sub-cluster in tumor and normal tissues, respectively.

To investigate the role of the sub-clusters identified in the present study, CIBERSORTx [15] analyses were performed to predict the fraction of each cell sub-cluster in samples from the TCGA LUSC cohort (Supplementary Fig. 3A-C). We found that tumor tissues showed higher infiltration levels of Tregs and exhausted CD8<sup>+</sup> T cells compared to normal tissues in the TCGA cohort (Fig. 2e), which suggested an immunosuppressive TME in LUSC. Compared with other immune-suppressive markers, T cell immunoglobulin and immunoreceptor tyrosine-based inhibitory motif domain (TIGIT) seemed to be more commonly expressed by Treg and exhausted CD8<sup>+</sup>T cells (Supplementary Fig. 2B). scRNA-seq data showed the expression of TIGIT was higher in tumor tissues compared with normal tissues(Fig. 2f). Furthermore, bulk-data from the TCGA showed similar results (Fig. 2g). Notably, the expression of TIGIT was positively correlated with the proportion of Treg and exhausted CD8<sup>+</sup>T in tumor region (Supplementary Fig. 2C). Immunohistochemical (IHC) staining of tumor tissues showed strongly positive staining, while normal tissues showed weak positive staining (Fig. 2h). Immunofluorescence (IF) staining confirmed that TIGIT was expressed by Tregs and exhausted CD8<sup>+</sup>T cells in LUSC tissues (Supplementary Fig. 2D). We also found that higher protein expression of TIGIT predicted a higher probability of recurrence after surgery in an independent cohort(P=0.018) (Fig. 2i). All the results suggested that TIGIT may be the potential target for prolonging the lifetime of LUSC patients.

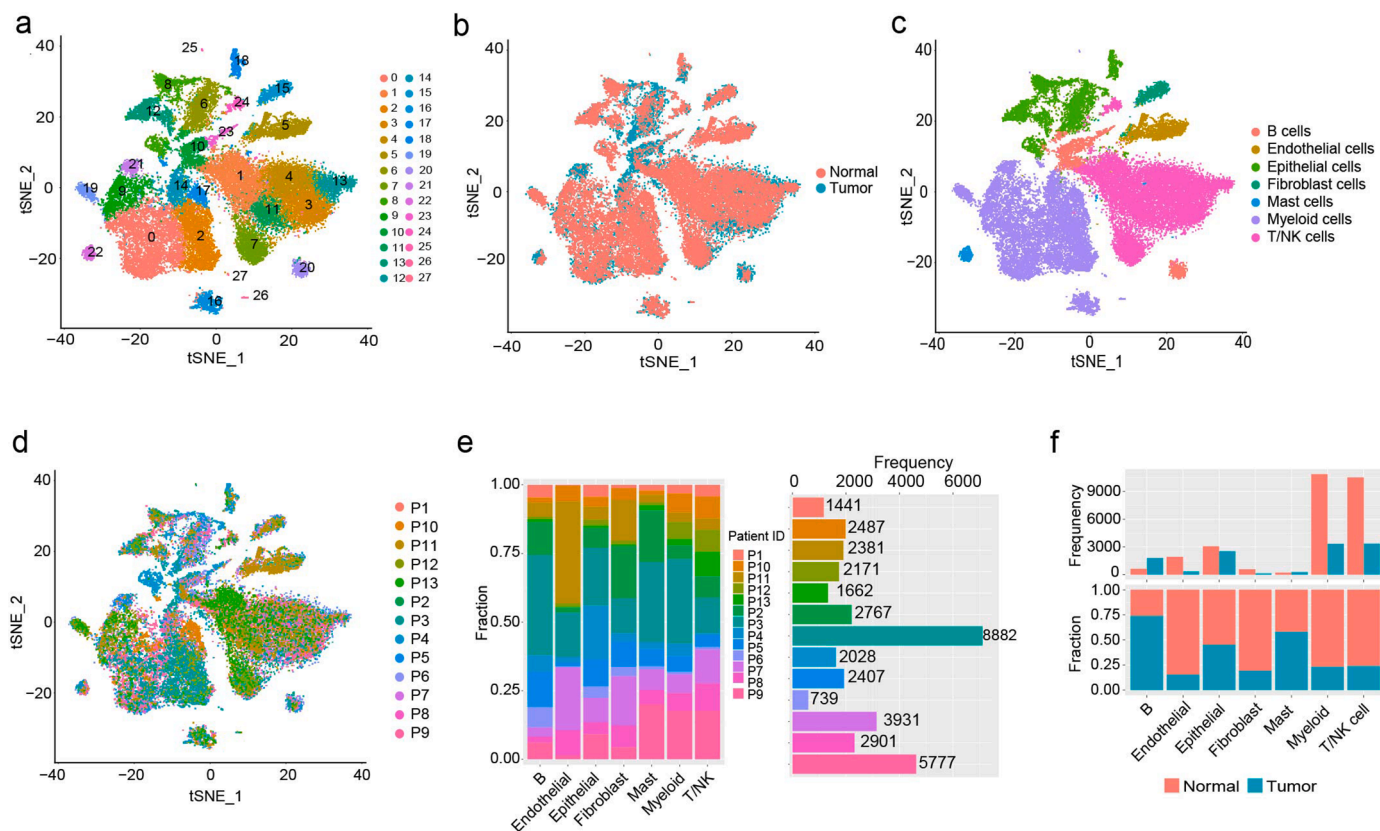


**Fig. 1.** Overview of the 39,574 single cells from lung squamous cell carcinoma (LUSC) and normal lung samples. a. Visualization of single-cell RNA-seq data of 39,574 cells clustered by t-SNE plot. b. t-SNE plot of single cells colored by the types of sample origin. c. t-SNE plot of single cells colored by the associated cell types according to gene expression pattern. d. t-SNE plot of single cells colored by patient origins. e. For each of the 7 major cell sub-clusters (left to right): the fraction of cells originating from the normal and tumor samples, and the number of cells from each sample. f. The frequency and proportion of each group of cells from malignant and normal tissues.

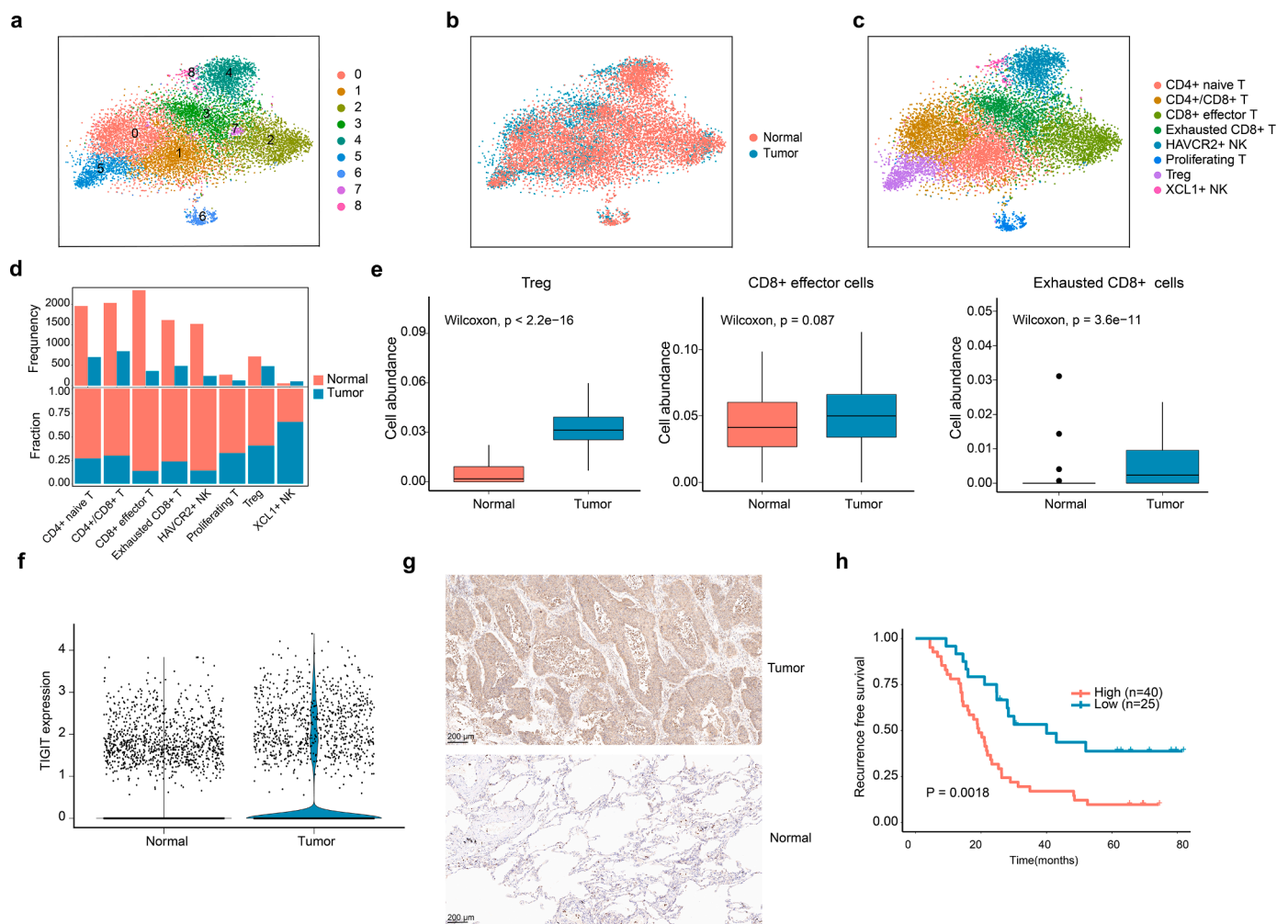


**Fig. 2.** TIGIT was highly expressed by Tregs and exhausted CD8<sup>+</sup> T cells. a. Re-clustering of T/NK cells by t-SNE plot. b. t-SNE plot of T/NK cells colored by the types of sample origin. c. t-SNE plot of T/NK cells colored by the types of cell subtypes. d. The frequency and proportion of each cell subtype from malignant and normal tissues. e. The abundance proportion of Tregs, CD8<sup>+</sup> effector T and exhausted CD8<sup>+</sup> T cells in the tumor and normal tissues from the TCGA cohort, respectively. (Difference between normal and tumor tissues was estimated by Wilcoxon-test). f. Violin plot showed the expression of TIGIT in T/NK cells from scRNA-seq data (Colored by sample origin). g. Immunohistochemical (IHC) stainings showed the expression of TIGIT in tumor and normal tissues. h. A higher expression level of TIGIT was correlated with worse recurrence-free survival from an independent cohort (Difference in recurrence-free survival between patients with high TIGIT expression and patients with low TIGIT expression was determined by log-rank test.).

#### *Tumor-associated neutrophils (TANs) act as an immunosuppressive contributor in TME*

Myeloid cells were re-clustered into 17 distinct sub-clusters (Fig. 3a), which were further classified as FABP4<sup>+</sup> macrophages (FABP4<sup>+</sup>M) (C0, C2, C6 and C16), mono/macrophage (C4 and C5), monocyte (C8 and C12), SEPP1<sup>+</sup> macrophages (SEPP1<sup>+</sup>M) (C1), SEPP1<sup>+</sup> macrophages (SPP1<sup>+</sup>M) (C3), neutrophil (C11), CD141<sup>-</sup>CD1c<sup>-</sup>DC (C10), CD1c<sup>+</sup>DC (C9), CLEC9A<sup>+</sup>DC (C13), GZMB<sup>+</sup>DC (C14) and LAMP3<sup>+</sup>DC (C15) based on gene their markers expression (Supplementary Fig. 4A-B and Supplementary Table 3).

We identified a cell population of neutrophils, characterized by the expression of CXCR2, CSF3R, CXCL8, and S100A8 (Fig. 3c, Supplementary Figs. 4A, B and 5A). We observed that almost all the neutrophils originated from tumor tissues (Fig. 3b and 3d), and CXCR2 was exclusively expressed by neutrophil (Supplementary Fig. 5A). Existing neutrophils were validated by IF and IHC stainings (Supplementary Fig. 5B, C). To delineate the roles of neutrophils played in TME, GO enrichment analysis was performed. As depicted in Supplementary Fig. 5D, cellular response to interferon-gamma, neutrophil degranulation and I-kappa B kinase/NF-κB signaling was enriched in neutrophils from normal tissues,

while negative regulation of inflammatory response and negative regulation of inflammatory response were enriched in neutrophils originated from tumor tissues. The proportion of neutrophils significantly increased in tumor tissues compared with normal tissues in the TCGA LUSC cohort (Fig. 3e). Moreover, neutrophils from tumor tissues showed lower module scores of inflammatory response and reactive oxygen species pathway and higher scores of TGF-β signaling and N2 phenotype neutrophil (Fig. 3f and Supplementary Table 4). Similar to macrophages classified into pro-tumor and antitumor properties, neutrophil was also categorized into two subtypes, anti-tumor (N1) and pro-tumor (N2) phenotype in TME [17]. N2 neutrophils, also known as tumor associated neutrophil (TAN), were involved in immune-suppressive TME [18], epithelial-mesenchymal transitions (EMT) [19], nuclear extracellular trap (NET) formation [20], which facilitate immune escape, tumor initial, growth, and metastasis [21,22]. Thus, we annotated the neutrophils from tumor tissues as TAN. In addition, we demonstrated that the cell abundance of TAN showed a significant correlation with the expression of CXCL8 and CXCR2, respectively (Fig. 3g). CXCL8 was a potent chemokine for neutrophils and recruited neutrophils into TME by CXCL8/CXCR2 axis [23,24]. CXCL8 was upregulated in tumor tissues compared with normal tissues (Supplementary Fig. 5E). Thus, we

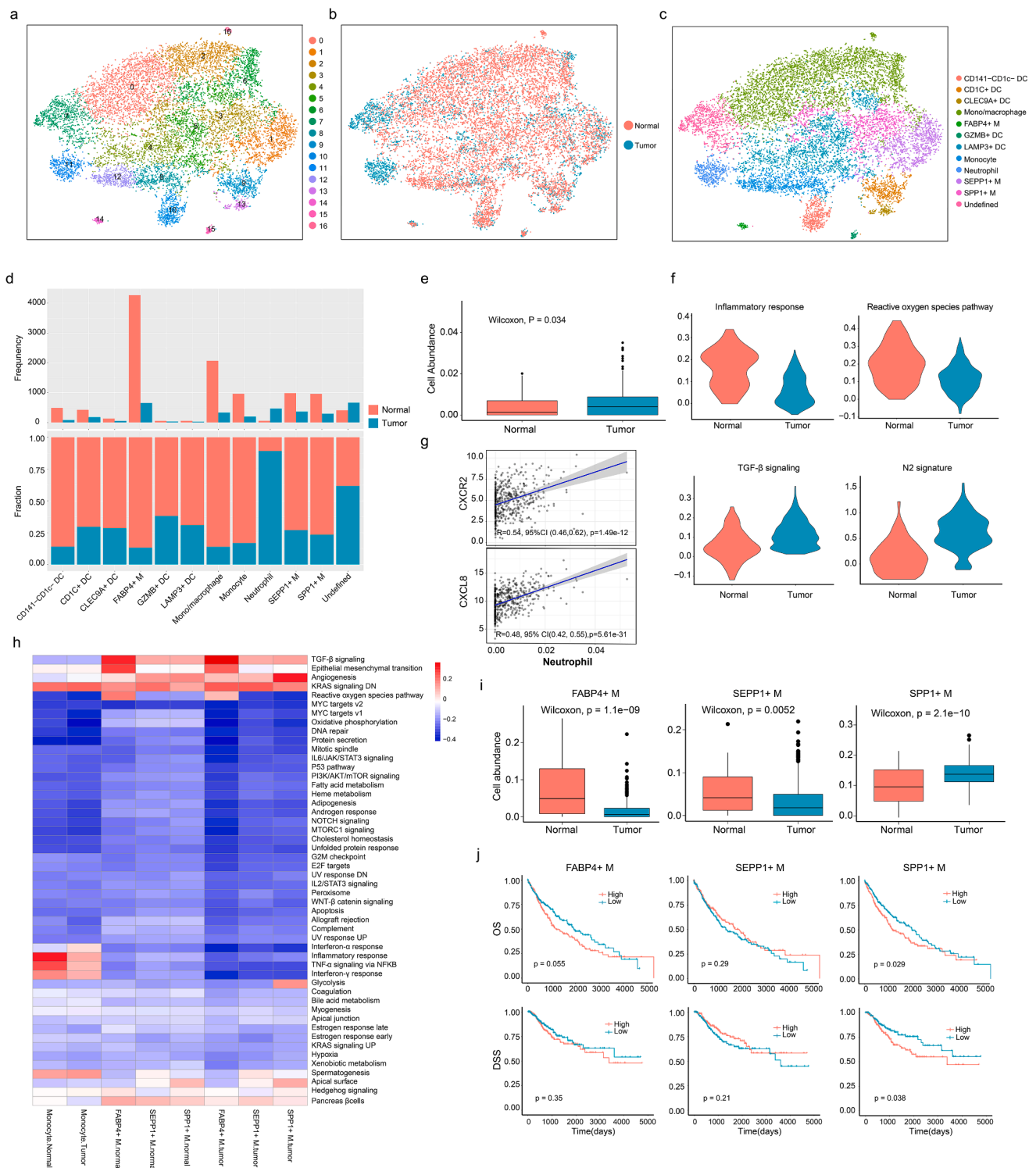


**Fig. 3.** Single-cell transcriptomic analysis reveals the transcriptome of myeloid cells in the microenvironment of LUSC. a. tSNE plot of myeloid cells color-coded by their associated clusters. b. tSNE plot of myeloid cells color-coded by their associated sample origins. c. tSNE plot of myeloid cells color-coded by cell subtypes established by marker genes. d. The frequency and proportion of each cell subtype from tumor and normal tissues. e. The boxplot showed the proportion of neutrophils in tumor and normal tissues, respectively, in the TCGA LUSC cohort. (The difference between normal and tumor tissues was calculated by Wilcoxon-test). f. Module scores of genes related to inflammation and N2 signature of neutrophil cluster from tumor and normal tissues, respectively. g. Correlation between neutrophil and expression level of CXCR2(top)/CXCL8(bottom) in TCGA LUSC cohort, respectively (The correlation coefficient and difference were calculated by Pearson-test). h. Heatmap shows the difference in pathway activities scored by GSVA per cell between different monocyte/macrophage groups. i. The boxplot showed the proportion of SPP1<sup>+</sup>M, SEPP1<sup>+</sup>M and FABP4<sup>+</sup>M from tumor and normal tissues, respectively, in the TCGA LUSC cohort. (Significance of difference between tumor and normal tissues was calculated by Wilcoxon-test). j. Association between cell abundance and patient survival from TCGA LUSC cohort (P value was calculated with log-rank test).

postulated that CXCL8 secreted by TANs recruited more neutrophils into the tumor region, and neutrophils polarized into TANs to promote tumor progression in TME.

In addition, we found that the expression of interleukin 1 receptor antagonist (IL1RN) was more commonly expressed by TANs from scRNA-seq data and was higher in tumor tissues compared to that in normal tissues from the TCGA LUSC cohort (Supplementary Fig. 5F–G). It was reported that IL1Ra counteracted the activation of pro-inflammatory signaling induced by IL-1 $\beta$  and acted as a potent mediator to inhibit the inflammatory response [25,26]. IHC staining from the human protein atlas (HPA) showed a higher expression of IL1Ra in tumor tissues compared with normal tissues (Supplementary Fig. 5H), and there was a significant correlation between the expression of IL1RN and the abundance of TAN in the TCGA LUSC cohort (Supplementary Fig. 5I). IF staining confirmed the existence of IL1Ra expressed by TANs in tumor tissues (Supplementary Fig. 5J). These results suggested that neutrophils might act as an immune-suppressive mediator via expressing IL1RN in TME.

#### Tumor-associated macrophages (TAM) was associated with worse survival

There are several subtypes of monocyte/macrophages identified in our study, namely FABP4<sup>+</sup> macrophage (FABP4<sup>+</sup> M) (CD68, LYZ, MARCO, APOC1 and FABP4), SEPP1<sup>+</sup> macrophage (SEPP1<sup>+</sup> M) (CD68, LYZ, MARCO, APOC1 and SEPP1), SPP1<sup>+</sup> macrophage (SPP1<sup>+</sup> M) (CD68, LYZ, MARCO, APOC1 and SPP1), monocyte (LYZ, VCAN, S100A8, S100A9 and S100A12) and mono/macrophage (CD68, LYZ, MARCO, VCAN, S100A8, S100A9). Mannose receptor C-type 1 (MRC1), also known as CD206, was highly expressed by FABP4<sup>+</sup> M, SEPP1<sup>+</sup> M, and SPP1<sup>+</sup> M (Supplementary Fig. 4C). CD206, a marker of tumor-associated macrophage (TAM), played pivotal roles in immunosuppressive TME and contributed in different ways to the various phases of carcinogenesis [27]. To further explore the potential roles of these sub-clusters, gene set variation analysis (GSVA) was performed. And we found that inflammatory response and TNF- $\alpha$  signaling via NF- $\kappa$ B were enriched in monocyte, while these enrichment scores were lower in FABP4<sup>+</sup> M, SEPP1<sup>+</sup> M and SPP1<sup>+</sup> M cells (Fig. 3h). Therefore, FABP4<sup>+</sup> M, SEPP1<sup>+</sup> M and SPP1<sup>+</sup> M might contribute to an immunosuppressive TME in LUSC. The proportion of SEPP1<sup>+</sup> M and FABP4<sup>+</sup> M decreased in tumor tissues compared with that in normal tissues, while the proportion of SPP1<sup>+</sup> M increased in tumor tissues (Fig. 3i).

In survival analysis from the TCGA cohort, the higher infiltration levels of SPP1<sup>+</sup> M cells were positively associated with shorter OS and DSS (Fig. 3j). We found that secreted phosphoprotein 1 (SPP1), encoding osteopontin, was highly expressed in the SPP1<sup>+</sup> M from tumor tissues, while the levels of SPP1 expression were relatively low in SPP1<sup>+</sup> M from normal tissues (Supplementary Fig. 6A), and bulk sequencing data from TCGA LUSC cohort showed a higher expression of SPP1 in tumor compared with that in tissues (Supplementary Fig. 6B). IHC staining confirmed higher expression of osteopontin in tumor tissues than normal tissues (Supplementary Fig. 6C), and IF staining confirmed that osteopontin was expressed by SPP1<sup>+</sup> M in LUSC tissues (Supplementary Fig. 6D). Recently, tumor-associated macrophage (TAM) was reported to be involved in tumor angiogenesis, extracellular matrix (ECM) receptor interaction, and tumor vasculature pathways [28]. In our study, we observed that TGF- $\beta$  signaling and angiogenesis pathways were enriched in SPP1<sup>+</sup> M in TME. Thus, SPP1<sup>+</sup> M might act as TAM to contribute to the formation of immunosuppressive TME and tumor progression in LUSC. All the findings suggested that targeting TAM might be the potential therapeutics for LUSC.

#### Five types of DC were identified in LUSC

Five types of dendritic cell (DC) were identified in our study, CD1C<sup>+</sup> DC cells (CD1C, CLEC10A, and FCER1A), LAMP3<sup>+</sup> DC (LAMP3, IDO1, CCR7 and FSCN1), GZMB<sup>+</sup> DC (GZMB, CXCR3, IRF4 and CLEC4C),

CLEC9A<sup>+</sup> DC and CD141<sup>-</sup> CD1C<sup>-</sup> DC (Supplementary Fig. 5 and Supplementary Table 3).

First, we found that the proportion of CD1C<sup>+</sup> DCs, GZMB<sup>+</sup> DCs and CLEC9A<sup>+</sup> DC were significantly higher in tumor tissues, while LAMP3<sup>+</sup> DCs and CD141<sup>-</sup> CD1C<sup>-</sup> DCs showed no significant difference between tumor and normal tissues (Fig. 4a). We found that the signatures of LAMP3<sup>+</sup> DC and CLEC9A<sup>+</sup> DC were associated with the signatures of Tregs (Supplementary Fig. 7), which suggested that LAMP3<sup>+</sup> DCs and CLEC9A<sup>+</sup> DCs recruited Tregs into the tumor region. Survival analyses showed that the high abundance of GZMB<sup>+</sup> DC and CD141<sup>-</sup> CD1C<sup>-</sup> DC predicted poor OS and DSS in the TCGA LUSC cohort (Fig. 4b). To further explore the roles the five subtypes of DCs played in TME, GO enrichment analyses were performed. All the DCs were involved in the immune response. However, CD141<sup>-</sup> CD1C<sup>-</sup> DCs were characterized by regulation of interleukin-6 production and mast cell degranulation and GZMB<sup>+</sup> DCs were characterized by regulation of response to endoplasmic reticulum stress and ubiquitin-dependent endoplasmic reticulum mediated degradation pathway (Fig. 4c).

#### Follicular B cells may contribute to immunosuppressive TME in LUSC

In our study, 2418 B lymphocyte and plasm cells were re-clustered (Fig. 5a), and five distinct clusters were identified. C0 was defined as IGHG1<sup>+</sup> plasm (IGHG1, IGHG1, CD79A) and C3 as TXNDC5<sup>+</sup> plasm (TXNDC5, JCHAIN, IGHG1 and CD79A). C2 was characterized as follicular B (CD79A, MS4A1, CD69 and CD24) (Fig. 5b, 5c and Supplementary Fig. 8A). C4 and C5 can not be defined due to their low quality. Fig. 5d showed the frequency and fraction of each cell subtype.

GO enrichment analyses were performed to investigate the functions of follicular B and plasm cells. We found that antigen processing and presentation of exogenous peptide antigen, response to interferon- $\gamma$  and immune response activating cell surface receptor signaling were enriched in follicular B cells (Supplementary Fig. 8B). For plasm cells, humoral immune response mediated by circulating immunoglobulin was enriched in both IGHG1<sup>+</sup> and TXNDC5<sup>+</sup> plasm cells. However, TXNDC5<sup>+</sup> plasm cells were characterized by protein N-linked glycosylation via asparagine. In the TCGA cohort, the proportion of follicular B and TXNDC5<sup>+</sup> plasm cells significantly increased in tumor tissues compared with that in normal tissues (Fig. 5e). In addition, the signatures of follicular B were correlated with the signatures of Tregs and LAMP3<sup>+</sup> DCs (Supplementary Fig. 8C), which suggested that follicular B may contribute to immunosuppressive TME in LUSC. However, the roles of plasm cells played in TME needed to be further validated. Trajectory analysis by monocle revealed that follicular B cells were located at the begin of the differentiation trajectory, while IGHG1<sup>+</sup> and TXNDC5<sup>+</sup> plasm cells were mainly located at the mid-terminal differentiation trajectory (Fig. 5f–5i). We could also found that “S4” state cells were tumor specific, which might be different from “S1” state cells. To explore it, we compared the follicular B cells derived from “S1” and “S4” state, and found that Interferon- $\gamma$  response was enriched in follicular B cells derived from “S1” state and TGF- $\beta$  signaling was enriched in follicular B cells derived from “S4” state (Supplementary Fig. 8D). All the results suggested follicular B cells were reprogrammed in TME and contributed to the formation of the immunosuppressive TME.

#### Composition of the stromal microenvironment of LUSC

The stromal cells were re-clustered, and several distinct clusters were obtained (Fig. 6a). And according to the marker genes, we identified EDN1<sup>+</sup> endothelial (C0, C3, C4 and C5), EDNRB1<sup>+</sup> endothelial (C1 and C6), CCL21<sup>+</sup> endothelial (C10), PDGFRA/B<sup>+</sup> fibroblast (C2 and C8), myofibroblast (C11), and fibroblast cells (C7 and C9) (Fig. 6c and Supplementary Fig. 9A). Fig. 6b, d presented the distribution and the proportion and frequency of each subtype. To investigate the potential role of various subtypes of fibroblast, survival analyses were performed. We found that higher infiltration levels of myofibroblast were closely

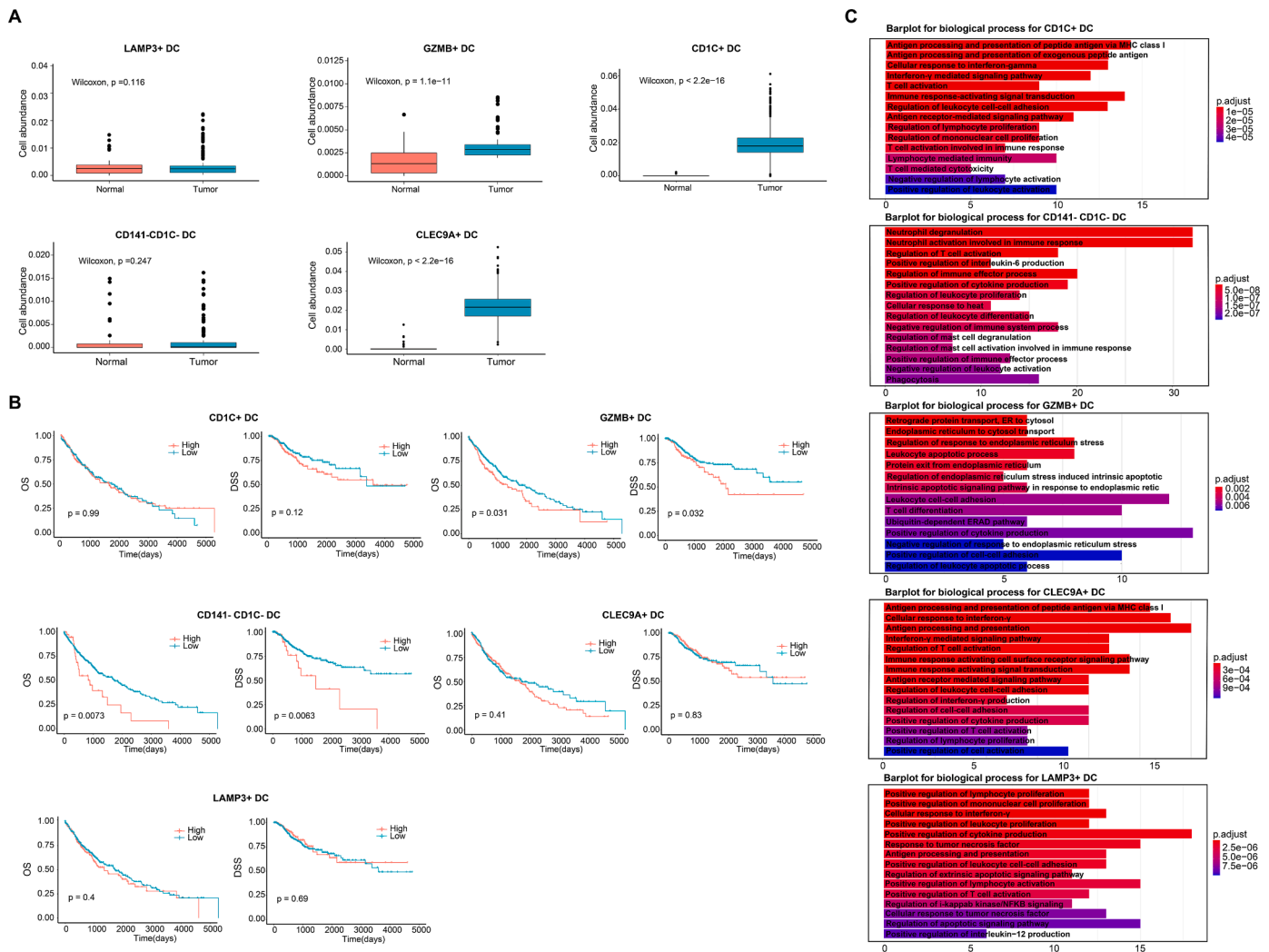


**Fig. 4.** Five types of DC were identified in LUSC. a. The difference in cell abundance of 5 types of DCs between tumor and normal tissues, respectively (The difference between normal and tumor tissues was calculated by Wilcoxon-test). b. Association between cell abundance and patient’s survival from TCGA LUSC cohort (P value was calculated with log-rank test). c. Enriched GO functions of upregulated genes in 5 types of DCs.

associated with poor OS and DSS (Fig. 6e), and there was a significant difference in myofibroblast abundance between normal and tumor tissues (Fig. 6f). Then, GO enrichment analysis revealed that extracellular matrix organization, regulation of angiogenesis, integrin-mediated signaling pathway, endothelial cell migration, TGF- $\beta$  receptor signaling pathway and mesenchymal cell differentiation were enriched in myofibroblast (Supplementary Fig. 9B). Furthermore, we also found that there was a significant positive correlation between the infiltration levels of myofibroblast and EDN1+ or EDNRB+ endothelial (Supplementary Fig. 9C), all of which suggested that myofibroblast was responsible for angiogenesis and stromal remodeling. IF stainings confirmed the existing myofibroblast in LUSC and normal tissues (Supplementary Fig. 9D) Tractory analysis revealed a tumor specific branch, which was mainly located at the end of differentiation tractory and could also be assigned as “S5” state cells (Fig. 6g-i). Various subtypes of fibroblast cells from normal tissues were mainly at the begin of differentiation tractory. To investigate the difference between fibroblast cells from normal tissues and fibroblast cells from tumor tissues, we found that pathways of allograft rejection, oxidative phosphorylation and graft versus host disease were enriched in fibroblast cells from normal tissues while ECM receptor interaction, inositol phosphate metabolism and pathways in cancer were enriched in fibroblast cells from tumor tissues (Supplementary Fig. 9E), all of which suggested that fibroblast cells were reprogrammed into tumor-promoting phenotype in TME. In

addition, myofibroblast cells were mainly located at the middle of differentiation tractory (Fig. 6a and 6j), which suggested that myofibroblast was differentiated from other fibroblast subtypes, and the process was known as fibroblast-to-myofibroblast transition (FMT) [29,30]. Butti et al. [30]. demonstrated that FMT was involved in increasing breast cancer aggressiveness.

*Constructing regulatory networks of immune cells in LUSC*

To explore the interaction networks between the cell subpopulations, we performed cell-cell communication analyses using CellphoneDB2 [31]. Notably, SPP1<sup>+</sup>M, SEPP1<sup>+</sup>M, PDGFRA/B<sup>+</sup> fibroblast and CD1C<sup>+</sup>DCs showed the most interactions with other cell types (Fig. 7a). And then, the SPP1<sup>+</sup>M-based regulatory networks were constructed. We observed disparities in the cell-cell interactions between normal and tumor tissues, such as SPP1-CD44, CD52-SIGLEC10, IL1RN-IL1B and CXCL8-CXCR2. Among these pairs, the pattern of the SPP1-CD44 ligand-receptor complex suggested the most functional interactions between SPP1<sup>+</sup>M and other cell types in TME (Fig. 7b). CD44 was a widely expressed ligand on the membrane of various types of cells (Fig. 7c, d) and was reported to be involved in tumor progression and cancer cell metastasis [32,33]. Osteopontin was reported to be involved in the proliferation, migration, and invasion of cancer cells [34,35], and silencing of SPP1 could suppress the progression of cancer cells [36].

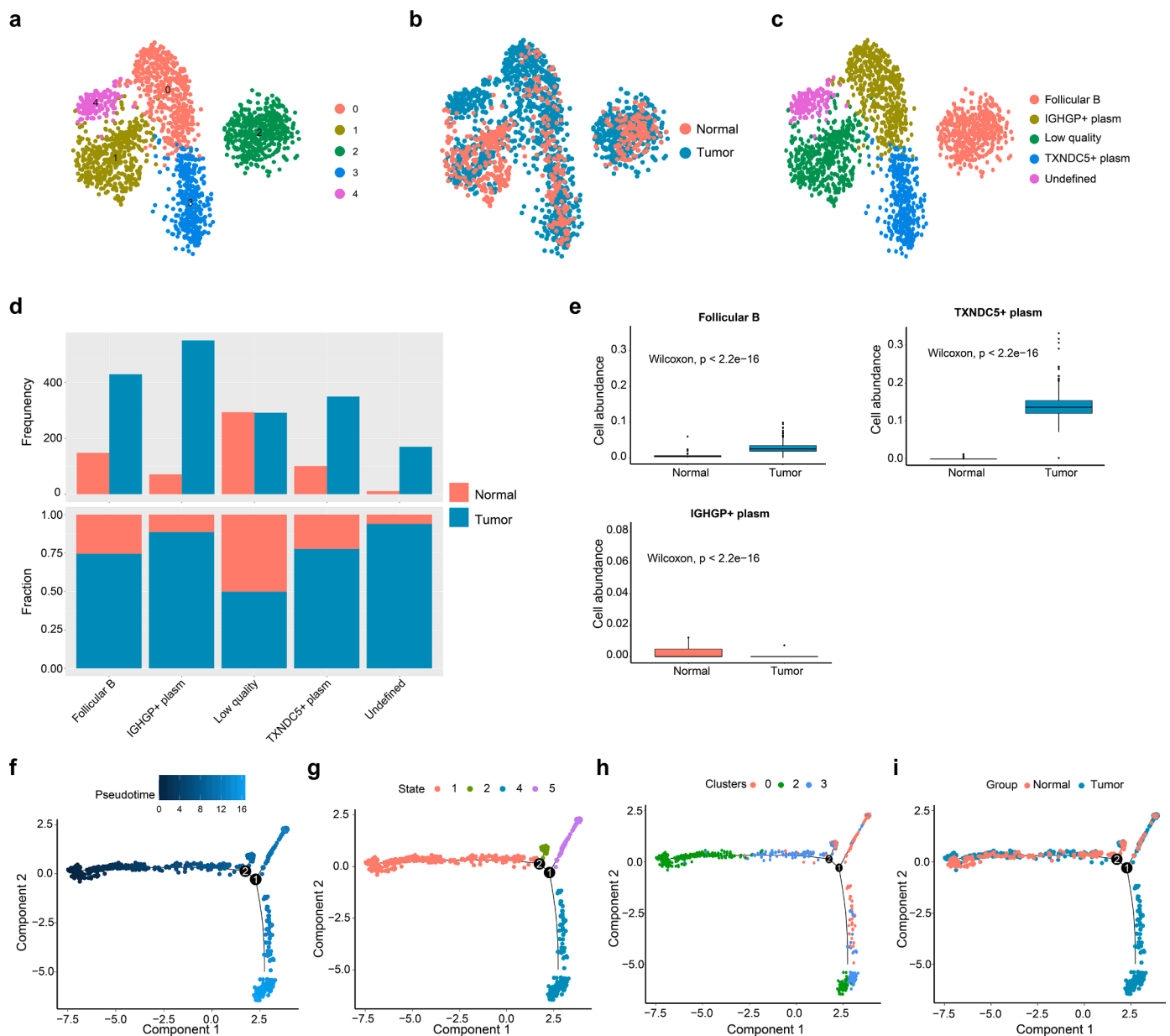


**Fig. 5.** Reclustering of follicular B and plasma cells. a. tSNE plot of B/plasm cells color-coded by their associated clusters. b. tSNE plot of B/plasm cells color-coded by their associated sample origins. c. tSNE plot of B/plasm cells color-coded by cell subtypes established by marker genes. d. The frequency and proportion of each cell subtype from tumor and normal tissues. e. The difference in cell abundance of 3 subtypes of B/plasm cells between tumor and normal tissues. f. Trajectory of differentiation predicted by monocle. g-i. Differentiation trajectory colored by state(g), clusters(h) and sample origin(i), respectively.

Osteopontin could suppress T cell activation via binding CD44 and contribute to immune tolerance in colon carcinoma [37]. These results suggested that SPP1<sup>+</sup>M promoted tumor progression and metastasis via the osteopontin/CD44 signaling pathway. All these results suggested that SPP-CD44 might be the promising target for overcoming LUSC.

Additionally, the SEPP1<sup>+</sup>M-based, FABP1<sup>+</sup>M-based, CD1C<sup>+</sup>DC-based and PDGFRA/B+ fibroblast based regulatory networks were also constructed. The disparities of the pair of SPP1-CD44 also exist in the SEPP1<sup>+</sup>M-based, FABP1<sup>+</sup>M-based, CD1C<sup>+</sup>DC-based and CD1C<sup>+</sup>DC-based regulatory networks(Supplementary Fig. 9). In PDGFRA/B+ fibroblast based regulatory networks, the regulatory patterns of FN1-a3b1 complex, COL6A2-a2b1 complex, COL6A3-a2b1 complex, COL6A3-a2b1 complex, COL6A1-a2b1 complex, COL1A2-a2b1 complex, COL5A2-a2b1 complex, FN1-a2b1 complex, COL3A1-a2b1 complex and COL1A1-a2b1 were upregulated in tumor tissues versus normal tissues. However, the ligand-receptor pairs of COL6A3-a10b1 complex,

COL6A2-a10b1 complex, COL6A2-a10b1 complex, COL1A1-a10b1 complex, COL3A1-a10b1 complex, FN1-a10b1 complex were downregulated in tumor tissues versus normal tissues.

**Discussion**

Although tremendous progress has been made in immunotherapy, there are still many LUSC patients who showed no response to it. Novel molecular targets or therapeutic strategies need to be further explored, which would be accelerated by a deep understanding of the TME. In our study, we analyzed single-cell transcriptome data, and we tried to depict a landscape of the cell components and construct the potential regulatory networks of immune cells in TME for LUSC. The atlas revealed the characteristics of immunosuppressive cells that facilitate the immune escape of tumor cells in LUSC. To the best of our knowledge, this provides the most comprehensive cellular interaction map of LUSC and a

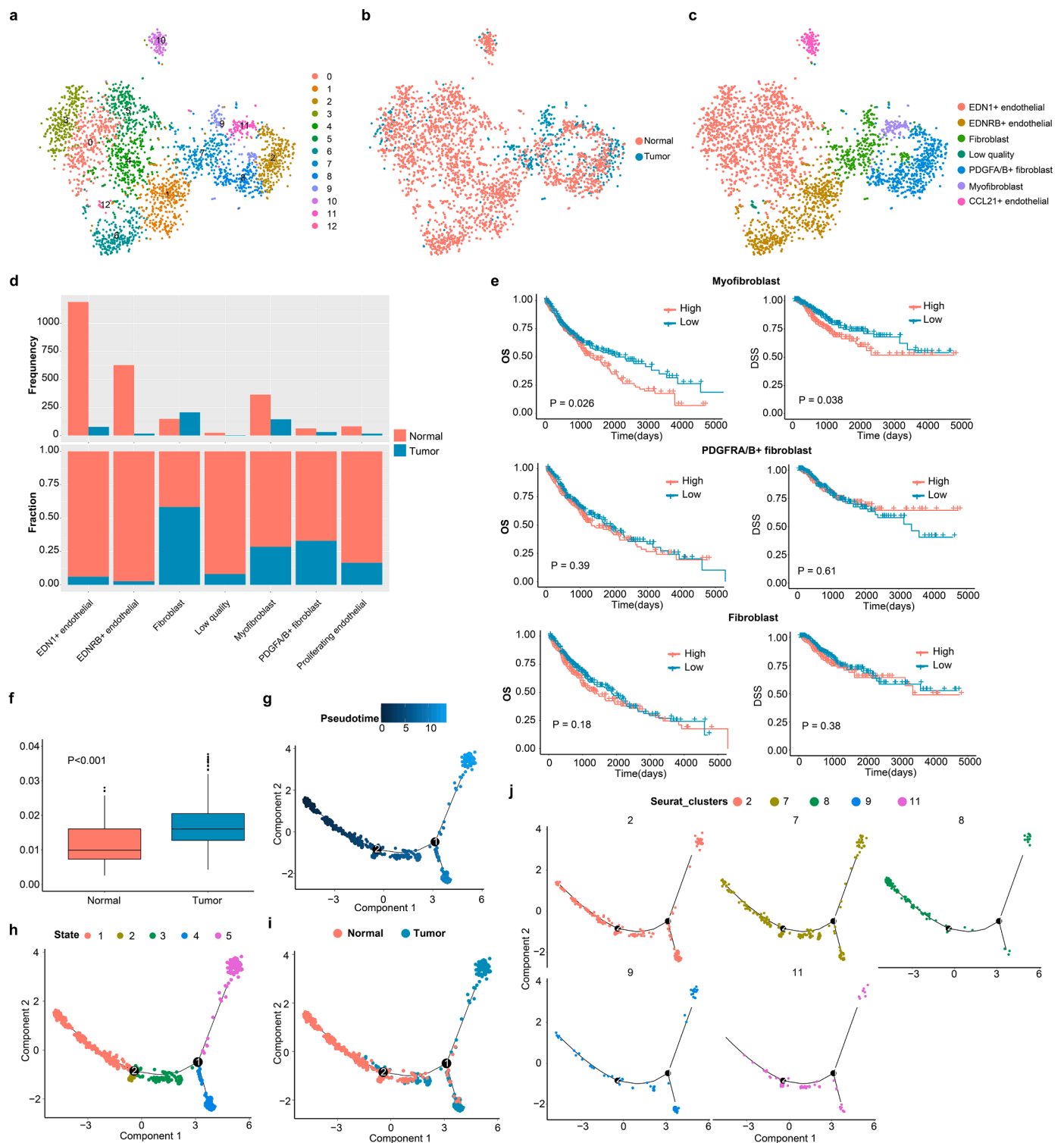


**Fig. 6.** Composition of the stromal microenvironment of LUSC. a. tSNE plot of fibroblast/endothelial cells color-coded by their associated clusters. b. tSNE plot of fibroblast/endothelial cells color-coded by their associated sample origins. c. tSNE plot of fibroblast/endothelial cells color-coded by cell subtypes. d. The frequency and proportion of each cell subtype from tumor and normal tissues. e. Association between cell abundance and patient survival from TCGA LUSC cohort (P value was calculated with log-rank test). f. The difference in cell abundance of myofibroblast between tumor and normal tissues (Significance of difference between tumor and normal tissues was calculated by Wilcoxon-test). g. The trajectory of differentiation predicted by monocle. h-j. Differentiation trajectory colored by state(h), sample origin(i) and clusters(j), respectively.

framework for future discoveries of molecular and cellular therapeutic targets for LUSC treatment.

We identified the immune checkpoint TIGIT that was commonly expressed by Tregs and exhausted CD8+T cells in tumor tissues, and the

higher expression of TIGIT was significantly associated with the higher proportion of Tregs and exhausted CD8+T cells. Published studies showed that TIGIT was associated with impaired function of tumor killing of NK, induced production of immunosuppressive cytokines



while CXCL8 was reported to recruit neutrophils to the tumor site via binding CXCR2 [43]. We observed that CXCR2<sup>+</sup>TANs were mainly located in the tumor region. Thus, a positive feedback loop may exist in TANs, namely TANs secreted CXCL8, and then CXCL8 recruited neutrophils to polarize into TANs. TANs were reported to be involved in protecting tumor cells from CD8<sup>+</sup>T and NK cell-mediated cytotoxicity [44], recruiting Tregs [45], and promoting tumor cell metastasis [46]. Thus, the infiltration of TANs was not only associated with refractoriness to immune checkpoint therapy but also tumor metastasis in TME.

We identified a cell population of myofibroblasts in our study, which was correlated with the survival of patients, and we also found that myofibroblasts were differentiated from PDGFRA/B<sup>+</sup> fibroblasts/fibroblasts. The process of fibroblast to myofibroblast transition (FMT) is reported to be facilitated by osteopontin in breast cancer, and the transition promotes tumor progression [30]. Besides, monocle analysis indicated that a branch of tumor-specific fibroblast subgroup cells ("S5" state), which were mainly located at end of differentiation trajectory. And pathways in cancer and ECM receptor interaction were enriched in "S5" state cells, while allograft rejection and graft versus host disease were enriched in "S1" state cells, which mainly originated from tumor tissues. All of these results suggested that fibroblast underwent phenotype reprogramming in TME, from participating in the immune response to the process of tumor facilitating, which known as cancer-associated fibroblast. CAF is recognized as a critical component of TME and is involved in ECM remodeling, metastasis, angiogenesis, maintenance of cancer stemness, the formation of immunosuppressive TME and drug resistance [47,48]. Thus, targeting myofibroblast or fibroblasts might be a choice for LUSC treatment.

Vilchez mercedes and his colleagues redefined the conception of "leader cells", which is responsible for path generation and interacting with and coordinating the motion of follower cells via physiological mechanisms [49]. TAMs are able to act as leader cells to remodel extracellular matrix for invasion of tumor cells depending on secreting proteases and TGF- $\beta$ , to induce genetic instability via producing ROS, to promote tumor cell proliferation by generating growth factors, and to suppress antitumoral adaptive immunity by expressing suppressive soluble and membrane molecules [27,49]. In our study, TGF- $\beta$  signaling and angiogenesis were enriched in SPP1<sup>+</sup>M, and SPP1<sup>+</sup>M showed a higher expression of CD206 and was correlated with the outcome of patients. Thus, SPP1<sup>+</sup>M contributed to the formation of immunosuppressive TME and the growth of tumor, which could be recognized as TAM. SPP1 was reported to be involved in mediating macrophage polarization [50,51]. TAM upregulated the expression of SPP1, and thus, we speculated that TAMs secreted osteopontin in TME and thus osteopontin accelerated the polarization into TAM from monocytes. CD44, one of the ligands of osteopontin, is a ubiquitously expressed surface glycoprotein [52], and activation of osteopontin/CD44 signaling was closely associated with dysfunction of CD8<sup>+</sup>T cells [37], initiations of metastasis [53], and facilitation tumor growth [54]. Moreover, SPP1<sup>+</sup>M from tumor tissues showed high expression of MMP9, MMP12, MMP14 and MMP19 (Supplementary Fig. 11), which may contribute to path generation for the invasion of tumor cells. Therefore, SPP1<sup>+</sup>M may act as leader cells interacting with other cells and creating low-resistance migration tracks for follower cells to promote the tumor progression in LUSC TME.

CellphoneDB analysis revealed that the pair of SPP1-CD44 was significantly upregulated in SPP1<sup>+</sup>M-based regulatory networks in TME, and the pair of SPP1-CD44 showed strong interactions with other types of cells in TME. The activation of SPP1/CD44 signaling is closely related to the dysfunction of CD8<sup>+</sup> cytotoxic T cells [37], the initiation of metastasis [53], and the promotion of tumor growth [54]. It has been reported that osteopontin can promote the proliferation and differentiation of B lymphocytes [55]. In addition, the study of Sharon et al. [56] showed that osteopontin could induce fibroblast remodeling through activating CD44, and knockout of SPP1 inhibited fibroblast activation and tumor growth. Therefore, comprehensive regulatory networks were

conceived based on the above-mentioned results (Fig. 7e). TME is a complicated and sophisticated cellular ecosystem. Tumor cells could not only escape from attacks by immune cells but also induced reprogramming of macrophages and fibroblasts, in turn, to support themselves. Tumor cells can directly or indirectly by "employing" leader cells (TAM, CAF, etc.) coordinating with follower cells to promote collective cancer invasion.

## Conclusion

We depicted the landscape of immune cells and constructed the regulatory networks in LUSC. The atlas revealed the characteristics of immunosuppressive cells that facilitate the immune escape of tumor cells in LUSC. To the best of our knowledge, this provides the most comprehensive cellular interaction map of LUSC and a framework for future discoveries of molecular and cellular therapeutic targets for LUSC treatment. Our study provides deep insight into cancer immunology and reveals potential therapeutic targets for the treatment of LUSC.

## Author contributions

B.H., Z.Z. and Q.G. conceived the idea.  
 B.H., L.Z., T.F., C.S., and R.H. collected the data.  
 B.H., J.X., Z.L., and S.P. finished the bioinformatics analysis.  
 D.L., H.M. and W.L. helped with immunofluorescence staining.  
 B.L., J.Y., and N.L. helped with immunohistochemical staining.  
 All authors reviewed and approved the manuscript.

## Funding

This work was supported by grants from the National Natural Sciences Foundation of China (Grant No. 81770095).

## Availability of data and materials

All relevant data can be acquired by contacting the correspondent author.

## Ethics approval and consent

Our study was approved by the ethics committee of Renmin Hospital of Wuhan University and all participants provided written informed consent.

## Supplementary figure legends

Supplementary Fig. 1. Feature plot showed the expression of cell markers for 7 major sub-clusters.

Supplementary Fig. 2. A. Featureplot showed the established marker genes for each sub-cluster. B. Featureplot showed the immunosuppressive markers for each sub-cluster. C. The correlation between TIGIT level and the proportion of Tregs, CD8<sup>+</sup>effector T and exhausted CD8<sup>+</sup> T, respectively (Coefficient was calculated with spearman correlation analysis). D-E. Immunofluorescence (IF) staining confirmed the existence of exhausted CD8<sup>+</sup>T cells and Tregs (n=26), respectively.

Supplementary Fig. 3. A. Workflow of the estimation of cell abundance established by CIBERSORTx. B. Heatmap of the signature matrix created by CIBERSORTx. C. Boxplot showed the abundance of each cell population established by CIBERSORTx.

Supplementary Fig. 4. A. Feature plot showed the expression of marker genes. B. Vlnlin plot showed the expression of marker genes. C. Violin and feature plot showed expression of MRC1.

Supplementary Fig. 5. A. Feature plot showed the expression of CXCR2 and CXCL8 split by sample origins, respectively. B. IHC staining of CXCR2 on formalin-fixed and paraffin-embedded slides for the independent tumor and normal biospecimens, respectively (n=26). C. IF

staining of S100A8, CSF3R and CXCR2 in tumor and normal lung tissues, respectively. D. Enriched GO functions of upregulated genes in neutrophils from tumor and normal tissues, respectively. E. IHC stainings showed expression of CXCL8 from HPA(left) and independent cohort (right), respectively. F. Violin plot showed the expression level of CXCL8 across sample origins from scRNA-seq data. G. Bulk-seq data from the TCGA LUSC cohort showed the expression level of IL1RN in tumor and normal tissues, respectively(The difference between normal and tumor tissues was calculated by Wilcoxon-test). H. IHC stainings showed expression of IL1RN from HPA(left) and independent cohort(right), respectively. I. The correlation between IL1RN level and the proportion of neutrophils in the tumor region. (Coefficient was calculated with Spearman correlation analysis). J. IF staining of CXCR2,CXCL8 and IL1Ra in tumor and normal lung tissues, respectively.

Supplementary Fig. 6. A. Violin plot showed expression of SPP1 in SPP1<sup>+</sup> M from tumor and normal tissues. B. Box plot showed the difference in the expression of SPP1 between tumor and normal tissues in the TCGA LUSC cohort. C. IHC staining showed the expression of osteopontin in tumor and normal tissues. D. IF staining confirmed the expression of CD68, CD206, and osteopontin in tumor and normal tissues, respectively. (n=26)

Supplementary Fig. 7. Correlation between Tregs and two types of DC(LAMP3<sup>+</sup>DC and CLEC9A<sup>+</sup>DC) subgroups in TCGA LUSC cohort, respectively.

Supplementary Fig. 8. A. Feature plot showed the marker genes for B/plasm cells. B. Enriched GO functions of upregulated genes in follicular B, IGHG<sup>+</sup>plasm and TXNDC5<sup>+</sup>plasm cells, respectively. C. Correlation between follicular B cells and Tregs (top)and LAMP3<sup>+</sup>DC(bottom) in TCGA LUSC cohort, respectively. D. GSEA analysis of hallmark pathways for “S1” state and “S4” state follicular B, respectively.

Supplementary Fig. 9. A. Feature plot showed the marker genes for fibroblast/endothelial cells B. Enriched GO functions of upregulated genes in myofibroblast, fibroblast and PDGFRA/B<sup>+</sup> fibroblast. C. Correlation between follicular B cells and END1<sup>+</sup>endothelial (left) and ENRB<sup>+</sup>endothelial cells (right) in TCGA LUSC cohort, respectively.D. IF staining confirmed expression of PDGFRB, RGS5 and  $\alpha$ -SMA in tumor region, respectively(n=26). E. GSEA analysis of hallmark pathways for “S1” state and “S5” PDGFRA/B<sup>+</sup>fibroblast/fibroblast, respectively.

Supplementary Fig. 10. Bubble plots show ligand-receptor pairs of molecules in CD1C<sup>+</sup>DCs-based, SEPP1<sup>+</sup>M-based, FABP4<sup>+</sup>M-based and PDGFA/B<sup>+</sup>fibroblast-based regulatory networks.

Supplementary Fig. 11. Violin plot showed the expression of MMP9, MMP12, MMP14 and MMP19 from scRNA-seq data, respectively (Colored by sample origin).

## Declaration of Competing Interest

All authors declare no competing interests.

## Acknowledgments

We thank Dr. Jianming Zeng(University of Macau), and all the members of his bioinformatics team, biotrainee, for generously sharing their experience and codes. We thank Dr. Zhenhua Zhang(Sun Yat-sen University) for generously sharing their experience and codes.

## Supplementary materials

Supplementary material associated with this article can be found, in the online version, at doi:10.1016/j.tranon.2022.101568.

## References

- [1] H. Sung, J. Ferlay, R.L. Siegel, et al., Global cancer statistics 2020: GLOBOCAN estimates of incidence and mortality worldwide for 36 cancers in 185 countries, *CA Cancer J. Clin.* 71 (3) (2021) 209–249.
- [2] R.S. Heist, M. Mino-Kenudson, L.V. Sequist, et al., FGFR1 amplification in squamous cell carcinoma of the lung, *J. Thorac. Oncol.* 7 (12) (2012) 1775–1780.
- [3] S.L. Wood, M. Pernemalm, P.A. Crosbie, et al., The role of the tumor-microenvironment in lung cancer-metastasis and its relationship to potential therapeutic targets, *Cancer Treat. Rev.* 40 (4) (2014) 558–566.
- [4] J.M. Pitt, A. Marabelle, A. Eggermont, et al., Targeting the tumor microenvironment: removing obstruction to anticancer immune responses and immunotherapy, *Ann. Oncol.* 27 (8) (2016) 1482–1492.
- [5] T. Baslan, J. Hicks, Unravelling biology and shifting paradigms in cancer with single-cell sequencing, *Nat. Rev. Cancer* 17 (9) (2017) 557–569.
- [6] A. Maynard, C.E. McCoach, J.K. Rotow, et al., Therapy-induced evolution of human lung cancer revealed by single-Cell RNA sequencing, *Cell* 182 (5) (2020) 1232–1251, e1222.
- [7] Y. Lavin, S. Kobayashi, A. Leader, et al., Innate immune landscape in early lung adenocarcinoma by paired single-cell analyses, *Cell* 169 (4) (2017) 750–765, e717.
- [8] D. Lambrechts, E. Wauters, B. Boeckx, et al., Phenotype molding of stromal cells in the lung tumor microenvironment, *Nat. Med.* 24 (8) (2018) 1277–1289.
- [9] N. Kim, H.K. Kim, K. Lee, et al., Single-cell RNA sequencing demonstrates the molecular and cellular reprogramming of metastatic lung adenocarcinoma, *Nat. Commun.* 11 (1) (2020) 2285.
- [10] R. Zilionis, C. Engblom, C. Pfirschke, et al., Single-cell transcriptomics of human and mouse lung cancers reveals conserved myeloid populations across individuals and species, *Immunity* 50 (5) (2019) 1317–1334, e1310.
- [11] Q. Song, G.A. Hawkins, L. Wudel, et al., Dissecting intratumoral myeloid cell plasticity by single cell RNA-seq, *Cancer Med.* 8 (6) (2019) 3072–3085.
- [12] T. Stuart, A. Butler, P. Hoffman, et al., Comprehensive integration of single-cell data, *Cell* 177 (7) (2019) 1888–1902, e1821.
- [13] M. Efremova, M. Vento-Tormo, S.A. Teichmann, et al., CellPhoneDB: inferring cell-cell communication from combined expression of multi-subunit ligand-receptor complexes, *Nat. Protoc.* 15 (4) (2020) 1484–1506.
- [14] Z. Chen, L. Zhou, L. Liu, et al., Single-cell RNA sequencing highlights the role of inflammatory cancer-associated fibroblasts in bladder urothelial carcinoma, *Nat. Commun.* 11 (1) (2020) 5077.
- [15] A.M. Newman, C.B. Steen, C.L. Liu, et al., Determining cell type abundance and expression from bulk tissues with digital cytometry, *Nat. Biotechnol.* 37 (7) (2019) 773–782.
- [16] A. Asplund, P.H. Edqvist, J.M. Schwenk, et al., Antibodies for profiling the human proteome: the human protein atlas as a resource for cancer research, *Proteomics* 12 (13) (2012) 2067–2077.
- [17] Z.G. Fridlender, J. Sun, S. Kim, et al., Polarization of tumor-associated neutrophil phenotype by TGF- $\beta$ : “N1” versus “N2” TAN, *Cancer Cell*, 16 (3) (2009) 183–194.
- [18] S. Nagaraj, A.G. Schrum, H.I. Cho, et al., Mechanism of T cell tolerance induced by myeloid-derived suppressor cells, *J. Immunol.* 184 (6) (2010) 3106–3116.
- [19] G.Y. Liou, P. Storz, Reactive oxygen species in cancer, *Free Radic. Res.* 44 (5) (2010) 479–496.
- [20] L. Wu, S. Saxena, M. Awaji, et al., Tumor-associated neutrophils in cancer: going pro, *Cancers* 11 (4) (2019) (Basel).
- [21] J.D. Spicer, B. McDonald, J.J. Cools-Lartigue, et al., Neutrophils promote liver metastasis via Mac-1-mediated interactions with circulating tumor cells, *Cancer Res.* 72 (16) (2012) 3919–3927.
- [22] J.A. Joyce, J.W. Pollard, Microenvironmental regulation of metastasis, *Nat. Rev. Cancer* 9 (4) (2009) 239–252.
- [23] R. Ogawa, T. Yamamoto, H. Hirai, et al., Loss of SMAD4 promotes colorectal cancer progression by recruiting tumor-associated neutrophils via the CXCL1/8-CXCR2 axis, *Clin. Cancer Res.* 25 (9) (2019) 2887–2899.
- [24] Z.P. Peng, Z.Z. Jiang, H.F. Guo, et al., Glycolytic activation of monocytes regulates the accumulation and function of neutrophils in human hepatocellular carcinoma, *J. Hepatol.* 73 (4) (2020) 906–917.
- [25] J. Sehouli, A. Mustea, D. Kongsen, et al., Polymorphism of IL-1 receptor antagonist gene: role in cancer, *Anticancer Res.* 22 (6A) (2002) 3421–3424.
- [26] W.P. Arend, C. Gabay, Physiologic role of interleukin-1 receptor antagonist, *Arthritis Res.* 2 (4) (2000) 245–248.
- [27] M.R. Galdiero, G. Marone, A. Mantovani, Cancer inflammation and cytokines, *Cold Spring Harb. Perspect. Biol.* 10 (8) (2018).
- [28] L. Zhang, Z. Li, K.M. Skrzypczynska, et al., Single-cell analyses inform mechanisms of myeloid-targeted therapies in colon cancer, *Cell* 181 (2) (2020) 442–459, e429.
- [29] H. Lin, C. Wu, F. Zhu, et al., Anti-fibrotic effect of iguratimod on pulmonary fibrosis by inhibiting the fibroblast-to-myofibroblast transition, *Adv. Med. Sci.* 65 (2) (2020) 338–347.
- [30] R. Butti, R. Nimma, G. Kundu, et al., Tumor-derived osteopontin drives the resident fibroblast to myofibroblast differentiation through twist1 to promote breast cancer progression, *Oncogene* 40 (11) (2021) 2002–2017.
- [31] R. Vento-Tormo, M. Efremova, R.A. Botting, et al., Single-cell reconstruction of the early maternal-fetal interface in humans, *Nature* 563 (7731) (2018) 347–353.
- [32] C. Chen, S. Zhao, A. Karnad, et al., The biology and role of CD44 in cancer progression: therapeutic implications, *J. Hematol. Oncol.* 11 (1) (2018) 64.
- [33] H. Roedig, R. Damiescu, J. Zeng-Brouwers, et al., Danger matrix molecules orchestrate CD14/CD44 signaling in cancer development, *Semin. Cancer Biol.* 62 (2020) 31–47.
- [34] H. Tang, J. Chen, X. Han, et al., Upregulation of SPP1 is a marker for poor lung cancer prognosis and contributes to cancer progression and cisplatin resistance, *Front. Cell Dev. Biol.* 9 (2021), 646390.
- [35] J. Wang, F. Hao, X. Fei, et al., SPP1 functions as an enhancer of cell growth in hepatocellular carcinoma targeted by miR-181c, *Am. J. Transl. Res.* 11 (11) (2019) 6924–6937.

- [36] Q. Zhang, L. Li, Y. Lai, et al., Silencing of SPP1 suppresses progression of tongue cancer by mediating the PI3K/Akt signaling pathway, *Technol. Cancer Res. Treat.* 19 (2020), 1533033820971306.
- [37] J.D. Klement, A.V. Paschall, P.S. Redd, et al., An osteopontin/CD44 immune checkpoint controls CD8<sup>+</sup> T cell activation and tumor immune evasion, *J. Clin. Invest.* 128 (12) (2018) 5549–5560.
- [38] N.A. Manieri, E.Y. Chiang, J.L. Grogan, TIGIT: a key inhibitor of the cancer immunity cycle, *Trends Immunol.* 38 (1) (2017) 20–28.
- [39] J.M. Chauvin, H.M. Zarour, TIGIT in cancer immunotherapy, *J. Immunother. Cancer* 8 (2) (2020).
- [40] D. Rodriguez-Abreu, M.L. Johnson, M.A. Hussein, et al., Primary analysis of a randomized, double-blind, phase II study of the anti-TIGIT antibody tiragolumab (tira) plus atezolizumab (atezo) versus placebo plus atezo as first-line (1L) treatment in patients with PD-L1-selected NSCLC (CITYSCAPE), *J. Clin. Oncol.* 38 (15) (2020) 9503.
- [41] J. Kargl, S.E. Busch, G.H. Yang, et al., Neutrophils dominate the immune cell composition in non-small cell lung cancer, *Nat. Commun.* 8 (2017) 14381.
- [42] J. Leach, J.P. Morton, O.J. Sansom, Neutrophils: homing in on the myeloid mechanisms of metastasis, *Mol. Immunol.* 110 (2019) 69–76.
- [43] S. de Oliveira, C.C. Reyes-Aldasoro, S. Candel, et al., Cxcl8 (IL-8) mediates neutrophil recruitment and behavior in the zebrafish inflammatory response, *J. Immunol.* 190 (8) (2013) 4349–4359.
- [44] A. Teijeira, S. Garasa, M. Gato, et al., CXCR1 and CXCR2 chemokine receptor agonists produced by tumors induce neutrophil extracellular traps that interfere with immune cytotoxicity, *Immunity* 52 (5) (2020) 856–871, e858.
- [45] I. Mishalian, R. Bayuh, E. Eruslanov, et al., Neutrophils recruit regulatory T-cells into tumors via secretion of CCL17—a new mechanism of impaired antitumor immunity, *Int. J. Cancer* 135 (5) (2014) 1178–1186.
- [46] S. Tabaries, V. Ouellet, B.E. Hsu, et al., Granulocytic immune infiltrates are essential for the efficient formation of breast cancer liver metastases, *Breast Cancer Res.* 17 (2015) 45.
- [47] M. Bartoschek, N. Oskolkov, M. Bocci, et al., Spatially and functionally distinct subclasses of breast cancer-associated fibroblasts revealed by single cell RNA sequencing, *Nat. Commun.* 9 (1) (2018) 5150.
- [48] T. Liu, C. Han, S. Wang, et al., Cancer-associated fibroblasts: an emerging target of anti-cancer immunotherapy, *J. Hematol. Oncol.* 12 (1) (2019) 86.
- [49] S.A. Vilchez Mercedes, F. Bocci, H. Levine, et al., Decoding leader cells in collective cancer invasion, *Nat. Rev. Cancer* (2021).
- [50] Y. Zhang, W. Du, Z. Chen, et al., Upregulation of PD-L1 by SPP1 mediates macrophage polarization and facilitates immune escape in lung adenocarcinoma, *Exp. Cell. Res.* 359 (2) (2017) 449–457.
- [51] K. Shirakawa, J. Endo, M. Kataoka, et al., IL (Interleukin)-10-STAT3-Galectin-3 axis is essential for osteopontin-producing reparative macrophage polarization after myocardial infarction, *Circulation* 138 (18) (2018) 2021–2035.
- [52] H.R. Moorman, D. Poschel, J.D. Klement, et al., Osteopontin: a key regulator of tumor progression and immunomodulation, *Cancers* 12 (11) (2020) (Basel).
- [53] M. Ahmed, J.L. Sottnik, G.M. Dancik, et al., An osteopontin/CD44 Axis in RhoGDI2-mediated metastasis suppression, *Cancer Cell* 30 (3) (2016) 432–443.
- [54] A. Pietras, A.M. Katz, E.J. Ekstrom, et al., Osteopontin-CD44 signaling in the glioma perivascular niche enhances cancer stem cell phenotypes and promotes aggressive tumor growth, *Cell Stem Cell* 14 (3) (2014) 357–369.
- [55] J. Iizuka, [Relationship between osteopontin expression and autoimmune disease—analysis of osteopontin expressed in transgenic mice], *Hokkaido Igaku Zasshi* 73 (5) (1998) 487–495.
- [56] Y. Sharon, Y. Raz, N. Cohen, et al., Tumor-derived osteopontin reprograms normal mammary fibroblasts to promote inflammation and tumor growth in breast cancer, *Cancer Res.* 75 (6) (2015) 963–973.